

Hydroxyapatite/titania nanocomposites derived by combining high-energy ball milling with spark plasma sintering processes

Yu, L. G.; Que, Wenxiu; Khor, Khiam Aik; Xu, Jinling

2008

Que, W., Khor, K. A., Xu, J., & Yu, L. G. (2008). Hydroxyapatite/titania nanocomposites derived by combining high-energy ball milling with spark plasma sintering processes. *Journal of the European Ceramic Society*, 28(16), 3083-3090.

<https://hdl.handle.net/10356/94257>

<https://doi.org/10.1016/j.jeurceramsoc.2008.05.016>

© 2008 Elsevier Ltd. This is the author created version of a work that has been peer reviewed and accepted for publication by *Journal of the European Ceramic Society*, Elsevier Ltd. It incorporates referee's comments but changes resulting from the publishing process, such as copyediting, structural formatting, may not be reflected in this document. The published version is available at: [DOI: <http://dx.doi.org/10.1016/j.jeurceramsoc.2008.05.016>].

Downloaded on 09 Apr 2024 15:59:38 SGT

Hydroxyapatite/titania nanocomposites derived by combining high-energy ball milling with spark plasma sintering processes

Wenxiu Que ^{a, b, *} K. A. Khor ^b, J. L. Xu ^b, and L. G. Yu ^b

^a *Electronic Materials Research Laboratory, School of Electronic & Information Engineering,*

Xi'an Jiaotong University, Xi'an 710049, Shaanxi, People's Republic of China

^b *School of Mechanical and Aerospace Engineering, Nanyang Technological University, Nanyang Avenue, Singapore 639798, Singapore*

Abstract

Hydroxyapatite-reinforced nanocomposites with titania nanocrystals addition are prepared by a homogeneous mixing of nano-sized hydroxyapatite and titania nanocrystals based on high-energy ball milling and spark plasma sintering processes. The microstructural and mechanical properties of the HA/titania nanocomposites are studied by X-ray diffractometry analysis, Raman spectrometry, and scanning electron microscopy. The hardness and Young's modulus of the nanocomposites are characterized by a nanoindenter and they show that the incorporation of the titania nanocrystals improves the mechanical properties of the nanocomposites obviously and the improvement should be ascribed to the main solitary effect of the ceramic as additives as well as a denser nanocomposite due to combining high-energy ball milling with spark plasma sintering techniques. The bioactivity of the titania/HA nanocomposite is evaluated by immersing the SPS compact disk in the simulated body fluid (SBF) and the results indicate that the bioactivity of the nanocomposite is related to the addition of titania by inducing apatite nucleation on the sample's surface after being immersed in SBF.

Keywords: Milling; Nanocomposites; X-ray-methods; Mechanical properties; Biomedical applications

1. Introduction

Hydroxyapatite (HA), in bulk and granular forms with dense and porous structures, is widely used as bone spacers and fillers in clinical applications due to its biological and chemical similarity to the inorganic phases of bones and teeth. However, its intrinsic mechanical properties of low strength and high brittleness which can lead to instability and unsatisfactory duration of the implant in the presence of body fluids and local loading.^{1,2} It is necessary for a successful application of HA ceramics in load-bearing areas of the human body that HA should be strengthened. One attractive

* To whom correspondence should be addressed. Telephone: 86-29-82668679. Fax: 86-29-82668794.
E-mail: wxque@mail.xjtu.edu.cn.

way to overcome these mechanical limitations is to use bioactive HA as ceramic/metal composites so as to achieve the necessary mechanical strength and bioactive properties at the same time,^{3,4} which include that the incorporation of bioinert ceramics and the addition of biocompatible glass into HA matrix.⁵⁻⁷ As have been reported that titania and HA represent a good combination for functionally graded materials providing a gradient of bioactivity and good mechanical properties.⁸ Therefore, the addition of titania particles to HA materials has attracted considerable attention in recent years, which is based on the assumption that titania is able to enhance osteoblast adhesion and induce cell growth.⁹⁻¹² Especially, recent researchers have proved that adhesive and cohesive strength of the implants can be increased significantly by combining HA and titania as reinforcing additives.¹³⁻¹⁵ These results indicate that the addition of titania into HA has a major effect on the HA structure and a positive effect on HA properties. However, due to the addition of a secondary phase, the phase changes of the composites at a higher sintering temperature are possible to occur. Actually, the reinforcing mechanism of the secondary phase in HA matrix has yet to be convincingly disclosed and a good understanding of the composite forming mechanism and microstructure characterization should contribute considerably to the development of the reinforced bioceramic composites. Most of the work has been reported so far on bulk composite materials, but it is obvious that the use of nanoparticulate materials to attain more superior mechanical properties has been proposed.¹⁶ For example, nanocrystallized HA can promote osteoblast adhesion and proliferation as compared with conventionally crystallized HA.² It is also believed that nano-sized HA can improve the sintering kinetics due to higher surface area and hence improve mechanical properties¹⁷. In the present study, we report on the preparation and characterization of HA/titania nanocomposites obtained by a homogeneous mixing of nano-sized HA powders and nano-crystallized titania powders based on high-energy ball milling and spark plasma sintering (SPS) processes. The microstructural and mechanical properties of the HA/titania composites are presented and the bioactivity of the HA/titania composites is also evaluated through the simulated body fluid (SBF) immersion.

2. Experimental procedure

The fully crystallized HA powders were prepared by a wet chemical precipitation approach by reacting 0.3 mol of orthophosphoric acid (H_3PO_4) with 0.5 mol of calcium hydroxide [$\text{Ca}(\text{OH})_2$] solution till the pH of the mixed solution reached 8.0.^{18,19} After the complete mixing of the reactants, the mixed solution was stirred at room temperature for 2h and then let the settle overnight. The settled precipitate was spray-dried using L-12 Spray Dryer at a feed-rate of 2-3 kg/h. The spray-dried HA powders were sieved and the powders with a particle sized larger than 20 μm were sieved out. The powders with a particle size less than 20 μm were used as HA source of the HA/titania composites. Nanocrystalline TiO_2 powders were prepared by using a sol-gel technique. Titanium isopropoxide [$\text{Ti}(\text{OC}_3\text{H}_7)_4$, TIP] was used as the TiO_2 precursor, absolute ethanol (99.9%) used as solvent and nitric acid used as a catalyst controlling the PH of the solution. The matrix sol was prepared by two solutions. In the preparation of the solution I, TIP was first diluted with absolute ethanol under vigorous stirring for about 30 minutes. For solution II, absolute ethanol, deionized water, and nitric acid (HNO_3) were mixed together and used as the acidic catalyst for hydrolysis of TIP. Two solutions (solutions I and II) were then mixed by adding the acidic solution (solution II) drop wise to the TIP-ethanol solution (solution I). The final mixture solution was stirred for about 20 h at room temperature. The final composition of the

solution in a molar ratio was $\text{TIP:H}_2\text{O:NHO}_3 = 1:1:0.15$ and ethanol was 50 mol. The powders obtained from the sol that was poured into Petri dish and dried at room temperature for about 2 weeks were then directly put in the furnace and heated for 3 h at a temperature of 500°C . The particle size of the nanocrystalline TiO_2 powders was less than 50 nm. The composite powders of HA with the addition of 10% mol nanocrystalline titania powders as prepared above were well mixed through a mechanical blending process in a Fritsch Pulverisette 5 planetary high-energy ball milling system for up to 20 h in air at room temperature. A 250 ml tungsten carbide vial and 100 tungsten carbide balls with a diameter of 10 mm were used as a milling medium. The HA/titania nanocomposite powders with a weight of about 25 g were placed in the vial. The milling speed and time were set at 200 rpm and 20 h, respectively. After the milling process was stopped, the milled powders were collected from the vial.

Spark plasma sintering (SPS) system (Dr. Sinter 1050, Sumitomo Coal Mining, Japan) was used to sinter the composite powders. 0.7 -1.0 g of the nanocomposite powders were loaded without any pressure or sintering aids in a graphite die (13 mm in diameter) and punch unit. A low internal pressure (a few Pa) was applied at the beginning of the sintering experiment. The temperature was measured by a pyrometer on the surface of the graphite die cylinder. The internal pressure was controlled by a Pirani element. The displacement data were recorded from 600°C onwards. The heating rate was at 100°C and the sample was heated for 5 minutes at different temperatures of 900, 1000, 1100, and 1200°C .

The SBF was prepared following the route as reported in Ref.²⁰ and the concentration of the different ionic species is nearly equal to that of human blood plasma at physiological conditions. All SPS compacts (HA/TiO_2 composite specimens) were polished by 2000# silicon carbide paper and cleaned in the ultrasonic bath for 40 min before SBF immersion. SPS compact was then immersed in 10 ml of SBF for 3 days at 37°C with a pH of 7.4. The temperature was maintained employing a water bath. Upon removal from SBF, the SPS compacts were gently rinsed with deionized water and dried in air.

X-ray diffractometry (XRD), scanning electron microscopy (SEM), and Raman spectroscopy were used to study the microstructural and morphological properties of the SPS compacts. The phase characterization of the samples was performed using a Philips MPD 1880 X-ray diffraction with $\text{Cu K}\alpha$ radiation and operated at 40 kV and 30 mA from 20 to 60° at a scanning rate of $0.02^\circ/\text{s}$ and with a step size of 0.02° . A JEOL JSM-6340F scanning electron microscopy was used to reveal the morphological and structural features of the powders and SPS compact samples. Raman spectra of the samples were recorded at room temperature using a Renishaw Raman Imaging Microscope (UK). The excitation source is from a He-Ne laser attached to the microscope to provide a confocal illumination of the sample via a holographic beam splitter. Indentation experiments were carried out at room temperature and ambient atmosphere. The hardness and Young's modulus of the samples were characterized by a Nanoindenter XP (Nano instruments), and determined on the basis of the load-displacement curve. Hardness was calculated as the maximum applied load over the area of contact, which was calibrated as a function of contact depth up to 500 nm.

3. Results and discussion

Fig. 1 shows the SEM images of the TiO_2 nano-particles derived by the sol-gel technique under different magnification. It can be seen from the Fig.1 (a) that the size of

the TiO₂ particles is less than 50 nm in diameter and it is also confirmed by XRD that these TiO₂ particles have an anatase crystal structure. The nanocrystalline TiO₂ particles are used as the addition source for HA reinforcement at present study. Fig 1 (b) shows the spray-dried HA particles have nanostructures in a needle-shape with a length of about 80-120nm and a width of 20-30nm.

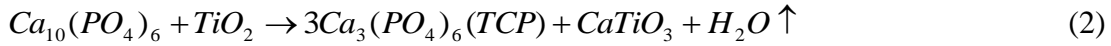
3.1 Phase composition

Fig. 2 shows the XRD patterns for the SPS compacts of the pure HA sintered at different temperatures. In order to compare conveniently, the XRD pattern of the pure HA is also presented in Fig. 2. It is noted that no changes in the diffraction peaks are observed for the samples sintered at temperatures of 900, 1000, and 1100°C, indicating HA structure in these samples is still not destroyed even with increase sintering temperature up to 1100°C. However, with further increase sintering temperature to 1200°C, apart from the HA phase is still able to observed clearly, alpha-tricalcium phosphate (Ca₃(PO₄)₂, α-TCP) and tetra-calcium phosphate (Ca₄P₂O₉, TTCP) are also found. These results indicate that the sample sintered at 1200°C appears to decompose due to the high sintering temperature during spark plasma procedure. Two other peaks appear at about 38.4 and 44.7° (marked as ‘*’ in Fig.2) are from aluminum (Al) of the sample holder material.¹⁶ The decomposition formula of HA can be used to understand the formation of the phase composition above-mentioned, which was also observed by others²¹



It should be mentioned here that TTCP and α-TCP only detected in the sample sintered at 1200°C. This may suggest that the formation of the different phases is due to the main result of extremely high spark plasma temperature (especially for a local temperature). The presence of TTCP suggests that further sintering of HA could result in further phase transformation to TTCP. This phenomenon was also reported in Ref.²² that only TTCP and α-TCP crystalline phases were observed and no other calcium phosphate phases were traced when HA treated at high temperature.

Fig. 3 shows the XRD patterns of the SPS compacts of the HA/titania nanocomposite sintered at different temperatures. It reveals that all samples mainly contain HA, TCP due to a decomposition of HA, rutile TiO₂ resulted from a phase transformation from anatase TiO₂ during sintering, and calcium titanate (CaTiO₃) phases, indicating that the HA structure starts being destroyed at the sintering temperature of 900°C with the formation of traces of TCP and CaTiO₃. With increase sintering temperature to 1100°C or above, a small amount of β-TCP phase, which is only detected in the samples sintered at 900 and 1000°C, transforms into α-TCP phase as observed in the samples sintered at 1100 and 1200°C. The appearance of the α-TCP phase suggests that further sintering of HA can result in further phase transformation. It has been widely reported that β-TCP phase is low-temperature polymorph of tricalcium phosphate and it will transform to high-temperature α-TCP phase.²³⁻²⁵ It should be noted that the transformation of β-TCP phase to α-TCP phase during SPS high sintering temperature may cause deleterious volume variation,⁵ which leads to decreasing the mechanical strength of the sample. It is evident that chemical reaction between HA and titania occurs during SPS sintering, which are indicated by the presence of CaTiO₃. The following formula can be used to understand the chemical reaction between HA and titania,



As compared with the pure HA, TTCP is not present in the HA/TiO₂ samples, indicating that the addition of TiO₂ to HA has beneficial effect in inhibiting further phase transformation of HA. Basically, TiO₂ is a chemically stable material with transformation from anatase to rutile at 400-1000°C. Actually, it has been pointed out that HA prefers to chemically react with anatase TiO₂ rather rutile TiO₂ when a composites are heated in air higher than 900°C,²⁴ while anatase TiO₂ was used in our experiment. The rutile phase is observed in Fig.3 suggests that transformation of anatase TiO₂ to rutile occurs during SPS high-temperature sintering. It can be concluded from above these results that some anatase TiO₂ transforms to rutile TiO₂ and the rest reacts with HA, the addition of TiO₂ can promote the decomposition of HA by to form CaTiO₃.

Raman spectra were used to further elucidate the structural properties of the reacting with HA

samples. Figs. 4 and 5 show the typical Raman spectra of the pure HA samples and HA/TiO₂ nanocomposites sintered at different temperatures, respectively. It can be clearly observed from Fig.4 that all SPS HA samples exhibit an obvious molecular character associated with the internal modes of PO₄³⁻ tetrahedral. Including that the peak centered at 438 cm⁻¹ is ascribed to the symmetric O-P-O bending mode (ν₂); the peak centered at 599 cm⁻¹ is from the component of asymmetric O-P-O bending mode (ν₄); a strong peak at about 960 cm⁻¹ is assigned to the non-degenerate symmetric P-O stretching mode (ν₁); and the fourth component of the ν₃ band is also observed at about 1046 cm⁻¹. Furthermore, the peak labeled at 3572 cm⁻¹, which is assigned to the stretching mode of hydroxyl group in HA, is weakened in all samples, and the peak at 631 cm⁻¹ from the hindered rotation mode of OH⁻ group in HA is not detected. This indicates that some hydroxyl groups in the samples are lost. It can be seen from the Raman spectrum of the SPS compacts of the pure HA sintered at 1000°C that the peaks at about 749, 830, 1337, and 1601 cm⁻¹ are observed, which are related to the carbon phases, but these peaks are not detected in the rest samples. A possible explanation is that the sample was contaminated during SPS process. Raman spectra of the HA/TiO₂ nanocomposite samples are shown in Fig.5. except for the stretching vibration bands of PO₄³⁻ labeled at 960 and 1046 cm⁻¹ are still observed in all studied samples, the bending modes of PO₄³⁻ labeled at 438 and 599 cm⁻¹ observed in the SPS HA samples are not detected here. However, a new peak of PO₄³⁻ at 1072 cm⁻¹ is traced and a band centered at around 770 cm⁻¹, which is assigned to HPO₄²⁻ or to γ₂ vibration in the CO₃²⁻ group, can be clearly observed with increase the sintering temperature (especially for the sample sintered at 1200°C) as compared to Fig. 4. These results indicate that the changes of PO₄³⁻ are thus revealed due to the appearance of the new phases, which have been concluded by XRD as shown in Fig.3. In addition to, the intensity of the band at 3572 cm⁻¹ from the stretching mode of hydroxyl group in HA decreases gradually with increase the sintering temperature. The transformation of HA into oxyhydroxyapatite or even oxyapatite would contribute to the decrease of the hydroxyl stretches as reported in Ref.¹³, indicating that more HA starts to decompose and transform into other phases by reacting with TiO₂ and further confirm the inference concluded from the XRD that the addition of TiO₂ can promote the decomposition of HA by reacting with HA to form CaTiO₃. It is also seen from Fig.5 that some peaks of rutile TiO₂ at 243, 450, and 611 cm⁻¹ can be clearly observed and the intensity of the peaks increases gradually and reaches the highest when the sintering temperature increases up to 1100°C. However, with further increase the sintering temperature to 1200°C, the intensity of the peaks

decreases greatly and is much more weak than that of the samples sintered below 1200°C, which can be understood that more titania reacts with HA at a higher sintering temperature. In addition, the peaks at about 1373 and 1402 cm⁻¹ observed only the sample sintered at 900°C are ascribed to the carbon phases due to contamination during SPS process.

3.2 Mechanical properties

Figs. 6 and 7 show the hardness and Young's modulus of the pure HA samples and HA/TiO₂ composites as a function of the sintering temperature, respectively. It can be seen from Fig. 6 that the hardness and Young's modulus of the HA samples increase gradually with an increase of the sintering temperature from 900 to 1100°C and the highest hardness and Young's modulus, which are 2.81 GPa and 45.33 GPa respectively, are obtained at sintering temperature of 1100°C. The increase of the hardness and Young's modulus by about 20% during the sintering temperature from 900 to 1100°C is ascribed to the densification of the sample during the sintering process. However, the hardness and Young's modulus of the sample starts to decrease with further increase sintering temperature to 1200°C. Especially, the value of the Young's modulus decreases by about 30%. The decrease of the hardness and Young's modulus should be related to a phase change due to the decomposition of the HA resulted from the high temperature sintering of 1200°C as shown in Fig.2. Furthermore, it is also possible that the increase of grain size from less than 1 to 5 μm contributes to the decrease of the hardness and Young's modulus, as reported by Ref.²⁴ that the mechanical properties of ceramics are sensitive to the grain sizes and a clear decrease in hardness is expected with larger grain size. The effect of TiO₂ incorporation on the mechanical properties of the pure HA is shown in Fig. 7. It is seen that the change of the hardness and Young's modulus of the TiO₂/HA composite with the sintering temperature is similar to that of the pure HA samples as shown in Fig. 6, which the values of the hardness and Young's modulus start to increase with the increase of the sintering temperature and reach a highest value at sintering temperature of 1100°C, and then decrease with further increase sintering temperature to 1200°C. It is noted from Fig. 7 that the values of the hardness and Young's modulus of the TiO₂/HA nanocomposites have an obvious improvement as compared with those of the pure HA sample, for example, the increase of the hardness and Young's modulus for the sample sintered at 1100°C are by about 23 % and 34 %, respectively, as compared to the HA sample sintered at 1100°C. That is to say, with the incorporation of TiO₂, the hardness increases from 2.81 GPa for pure HA to 3.45 GPa for the TiO₂/HA nanocomposite and the Young's modulus increases from 45.33 GPa to 60.69 GPa when the samples sintered at 1100°C. These results demonstrate that the addition of TiO₂ has a positive effect on improving both the hardness and the Young's modulus of the pure HA. Ref.²⁶ reported that for the composite without the consideration of the contribution of defects and chemical products, the Young's modulus of the composite satisfies the following linear relationship

$$E_c = V_p E_p + V_m E_m \quad (3)$$

Where E_c , E_m and E_p are the Young's modulus of the composite, matrix (HA) and particle (TiO₂), respectively, and V_p and V_m are the volume fraction of the matrix and particle, respectively. It can be believed that when sintering temperature is below 1100°C, the effect of an added interface a third phase, such as CaTiO₃, can be

considered as small. Thus, the improvement of the Young's modulus is contributed to the mere existence of TiO_2 . But with further increase sintering temperature to 1200°C , leading to the multi-phases in the composites resulted from chemical decomposition and mutual reaction between TiO_2 and HA, so that the Young's modulus decreases. These analyses can be further understood and supported by the results from XRD and Raman spectra. Moreover, it is also possible that the incorporation of TiO_2 induces a change of the residual stress inside HA, which may resulted in altering the Young's modulus. It should be mentioned here that the Young's modulus value of the samples as prepared in this paper is much higher than that of the earlier work reported in Ref.¹³, this should be ascribed to a more dense composite due to different preparation technique by combining high-energy ball milling with SPS technique. It can be concluded based on above these results that the addition of TiO_2 effectively increases the hardness and Young's modulus of the composite, considering the Young's modulus of TiO_2 is much higher than that of the pure HA, the change of the Young's modulus of the composite may be ascribed to the main solitary effect of the ceramic as additives and more dense composites. Furthermore, the density of the studied samples was measured by Melther Toledo with AG 245 mode at a temperature of 28.2°C and the average densities of the studied samples are listed in Table 1. It can be seen from the Table that the measured values of the HA samples and the HA/ TiO_2 composites increase gradually with increase the sintering temperature and then start to decrease with further increase the sintering temperature, which are similar to the change trend of the hardness and the Young's modulus with the sintering temperature. It is also can be observed that the density values of the composites sintered at different temperatures are smaller than those of the pure HA samples. The formation of the pores in the composites during SPS process as shown in Fig. 8, the formation of the multi-phases in the composite due to chemical decomposition, and mutual reaction between TiO_2 and HA should contribute to the decrease of the density values of the composites. Polished surface morphologies of the HA/ TiO_2 composites sintered at different temperature are shown in Fig. 8. Some pores can be clearly observed for the sample sintered at 900°C , more dense composite can be obtained with increase the sintering temperature to 1100°C . Obviously these results can be used to understand the change of the density values of the composites with sintering temperature. It can be concluded based on above these results that the sintering temperature of 1100°C is suitable for getting an ideal composite under the addition of 10% mol nanocrystalline TiO_2 powders.

3.3 *In vitro* behavior

The TiO_2 /HA compact sintered at 1100°C is immersed in SBF solution for *in vitro* behavior study. Fig. 9 shows the surface morphologies of the nanocomposite after three days of immersion in SBF. It is evident that on the surface of the nanocomposite compact, the apatite crystals can be clearly seen to grow after immersion in SBF, this layer looks like to be consisting of many nano-sized flaky crystallites with a dune-like morphology. Similar morphologies were also observed and reported in Refs.²⁷⁻²⁹. As reported in Refs.^{30, 31} that TiO_2 in the composite seems to have a good biocompatibility by inducing apatite nucleation on the sample's surface after being immersed in SBF. It is proposed that Ca^{2+} and PO_4^{4-} are released from the compact into the SBF solution, leading to the super-saturation of Ca^{2+} and PO_4^{4-} in the SBF, and then the Ca^{2+} exchanges with the H_3O^+ in the SBF to form Ti-OH group on the surface. The Ti-OH groups formed induce apatite nucleation, and the released Ca^{2+} and PO_4^{4-} ions accelerate apatite nucleation by increasing the ionic activity product of apatite in the fluid. Once

the apatite nuclei are formed, they can grow spontaneously by consuming the Ca^{2+} and PO_4^{4-} ions in the surrounding fluid. Thus, with the immersion time increases, these nuclei grow in size and form a layer to completely cover the original surface of the composite as seen from Fig.9. The apatite formed in SBF has been called bone-like due because its composition and structure are similar to the mineral phase of the bone and has been identified as the principal cause for promoting biocompatibility and bony tissue growth in biological environment.

4 Conclusions

TiO_2/HA nanocomposites were successfully prepared by combining high-energy ball milling with SPS processes. The phase composition, microstructure, mechanical properties, and in vitro behavior of the composites were also studied. The results indicated that HA in the composite starts to decompose into β -TCP due to the incorporation of TiO_2 , the HA reacts with TiO_2 to form CaTiO_3 , and β -TCP phase converted to α -TCP phase and anatase TiO_2 transformed to rutile TiO_2 with further increase in sintering temperature. It has been also demonstrated that the addition of TiO_2 has a positive effect on improving both the hardness and the Young's modulus of the HA and the improvement of the Young's modulus of the composite should be ascribed to the solitary effect of the ceramic as additives as well as a more dense composite due to combining high-energy ball milling with SPS technique. The bioactivities of the composite compact have been confirmed by in vitro test and the mechanism for apatite formation in SBF has been proposed.

References

- [1] M. C. Kuo, and S. K. Yen, The process of electrochemical deposited hydroxyapatite coatings on biomedical titanium at room temperature. *Mater. Sci. Eng. C*, 20, 153 (2002)
- [2] T. J. Webster, C. Ergun, R. H. Doremus, R. W. Siegel, and R. Bizios: Enhanced functions of osteoblasts on nanophase ceramics. *Biomaterials* 21, 1803 (2000).
- [3] K. Hayashi, N. Matsuguchi, K. Uenoyama, T. Kanemaru, and Y. Sugioka: Evaluation of metal implants coated with several types of ceramics as biomaterials. *J. Biomed. Mater. Res.* 23, 1247 (1989).
- [4] A. K. Lynn and D. L. Duquesnay: Hydroxyapatite-coated Ti-6Al-4V: Part 1: the effect of coating thickness on mechanical fatigue behaviour. *Biomaterials* 23, 1937 (2002).
- [5] W. Suchanek, M. Yashima, M. Kakihana, and M. Yoshimura: Hydroxyapatite ceramics with selected sintering additives. *Biomaterials* 18, 923 (1997).
- [6] B. Labat, A. Chamson, and J. Frey: Effects of α -alumina and hydroxyapatite coatings on the growth and metabolism of human osteoblasts. *J. Biomed. Mater. Res.* 29, 1397 (1995).
- [7] S. Gautier, E. Champion, and D. Bernache-Assollant: Toughening characterization in alumina platelet- hydroxyapatite matrix composites. *J. Mater. Sci. Mater. Med.* 10, 533 (1999).
- [8] T. Peltola, M. Patsi, H. Rahiala, I. Kangasniemi, and A. Yli-Urpo: Calcium phosphate induction by sol-gel-derived titania coatings on titanium substrates *in vitro*. *J. Biomed. Mater. Res.* 41, 504 (1998).
- [9] T. A. Vu and R. B. Heimann: Influence of the CaO/TiO₂ ratio on thermal stability of hydroxyapatite in the system Ca₅(PO₄)₃OH--CaO--TiO₂. *J. Mater. Sci. Lett.* 16, 1680 (1997).
- [10] P. A. Ramires, A. Romito, F. Cosentino, and E. Milella: The influence of titania/hydroxyapatite composite coatings on *in vitro* osteoblasts behaviour. *Biomaterials* 22, 1467 (2001).
- [11] P. A. Ramires, F. Cosentino, E. Milella, P. Torricelli, G. Giavaresi, and R. Giardino: *In vitro* response of primary rat osteoblasts to titania/hydroxyapatite coatings compared with transformed human osteoblast-like cells. *J. Mater. Sci., Mater. Med.* 13, 797 (2002).
- [12] M. H. Fathi, M. Salehi, A. Saatchi, V. Mortazavi, and S. B. Mosavi: *In vitro* corrosion behavior of bioceramic, metallic, and bioceramic-metallic coated stainless steel dental implants. *Dent. Mater.* 19, 188 (2003).
- [13] H. Li, K. A. Khor, and P. Cheang: Titanium dioxide reinforced hydroxyapatite coatings deposited by high velocity oxy-fuel spray. *Biomaterials* 23, 85 (2002).

- [14] Xu W, Hu WY, Li MH, Wen C. Sol-gel derived hydroxyapatite/titania biocoatings on titanium substrate. *Mater Lett* 2006; 60:1575-78.
- [15] X. F. Xiao, R. F Liu, and Y. Z. Zheng: Characterization of hydroxyapatite/titania composite coatings codeposited by a hydrothermal-electrochemical method on titanium. *Surf. Coat. Technol.* 200, 4406 (2006).
- [16] P. K. Chu, J. Y. Chen, L. P. Wang and N. Huang: Plasma-surface modification of biomaterials. *Mater. Sci. Eng. R* 36, 143 (2002).
- [17] S. Bose and S. K. Saha: Synthesis of Hydroxyapatite Nanopowders via Sucrose-Templated Sol-Gel Method. *J. Am. Ceram. Soc.* 86, 1055 (2003).
- [18] P. Cheang and K. A. Khor: Addressing processing problem associated with plasma spraying of hydroxyapatite coatings. *Biomaterials* 17, 537 (1996).
- [19] J. L. Xu, K. A. Khor, Z. L. Dong, Y. W. Gu, R. Kumar, and P. Cheang: Preparation and characterization of nano-sized hydroxyapatite powders produced in a radio frequency thermal plasma. *Mater. Sci. Eng. A* 374, 101 (2004).
- [20] T. Kukubo, H. Kushitani, S. Kitsugi, and T. Yammamuro: Solutions able to reproduce in vivo surface structure changes in bioactive glass-ceramic A-W. *J. Biomed. Mater. Res.* 24, 721 (1990).
- [21] W. Van Raemdonck, P. Ducheyne, and P. De Meester: Characterization of hydroxyapatite: before and after plasma spraying. *J. Mater. Sci. Med.* 13, 211 (2002).
- [22] M. A. Lopes, J. D. Santos, F. J. Monteriro, and J. C. Knowles: Glass-reinforced hydroxyapatite: a comprehensive study of the effect of glass composition on the crystallography of the composite. *J. Biomed. Mater. Res.* 39, 244 (1998).
- [23] W. Fix, H. Heymann, and R. Heinke: Subsolidus Relations in the System $2\text{CaO}-\text{SiO}_2-3\text{CaO}-\text{P}_2\text{O}_5$. *J. Am. Ceram. Soc.* 52, 346 (1969).
- [24] J. Weng, X. G. Liu, X. D. Zhang, and X. Y. Ji: Thermal decomposition of hydroxyapatite structure induced by titanium and its dioxide. *J. Mater. Sci. Lett.* 13, 159 (1994).
- [25] I. Rehman and W. Bonfield: Characterization of hydroxyapatite and carbonated apatite by photo acoustic FTIR spectroscopy. *J. Mater. Sci.: Mater. Med.* 8, 1 (1997).
- [26] L. J. Broutman: *Fracture and fatigue, composite materials*, Vol 5. New York: Academic Press, 1974.
- [27] J. Weng, Q. Liu, J. O. C. Wolke, X. Chang and K. Groom: Formation of characteristics of the apatite layer on plasma-sprayed hydroxyapatite coatings in simulated body fluid. *Biomaterials* 18, 1027 (1997).

- [28]Y. W. Gu, K. A. Khor, and P. Cheang: In vitro studies of plasma-sprayed hydroxyapatite/Ti-6Al-4V composite coating in simulated body fluid. *Biomaterials* 24, 1604 (2003).
- [29]S. C. Yu, K. P. Hariram, R. Kumar, P. Cheang, and K. A. Khor: In vitro apatite formation and its growth kinetics on hydroxyapatite/polyetheretherketone biocomposite. *Biomaterials* 26, 2342 (2005).
- [30]X. B. Zheng, M. H. Huang, and C. X. Ding: Bond strength of plasma-sprayed hydroxyapatite/Ti composite coatings, *Biomaterials* 21, 841 (2000).
- [31]H. B. Wen, J. R. de Wijin, F. Z. Cui, and K. de Groot: Preparation of bioactive Ti6Al4V surfaces by a simple method. *Biomaterials* 19, 215 (1998).

List of Tables

Table 1 Densities (g/cm^3) of the HA samples and HA/TiO₂ composite compacts sintered at different temperatures

List of Figures

- Fig. 1 SEM images of the sol-gel derived anatase TiO₂ (a) nanocrystals and HA (b) nanocrystals.
- Fig. 2 XRD patterns of the SPS compacts of the pure HA sintered at different temperatures
- Fig. 3 XRD patterns of the SPS compacts of the HA/titania composite sintered at different temperatures
- Fig. 4 Raman spectra of the pure HA samples sintered at different temperatures
- Fig. 5 Raman spectra of the HA/TiO₂ composites sintered at different temperatures
- Fig. 6 Hardness and Young's modulus of the pure HA samples as a function of the sintering temperature
- Fig. 7 Hardness and Young's modulus of the HA/TiO₂ composites as a function of the sintering temperature
- Fig. 8 Polished surface morphologies of the HA/TiO₂ composite sintered at 900°C, 1000°C, 1100°C after immersion in SBF for three days.
- Fig. 9 SEM surface morphology of the SPS compact of the HA/TiO₂ composite sintered at 1100°C after immersion in SBF for 3 days.

	Temperature (°C)			
	900	1000	1100	1200
HA	2.744	3.133	3.076	3.045
TiO ₂ /HA	2.956	2.981	2.983	2.737

Table 1

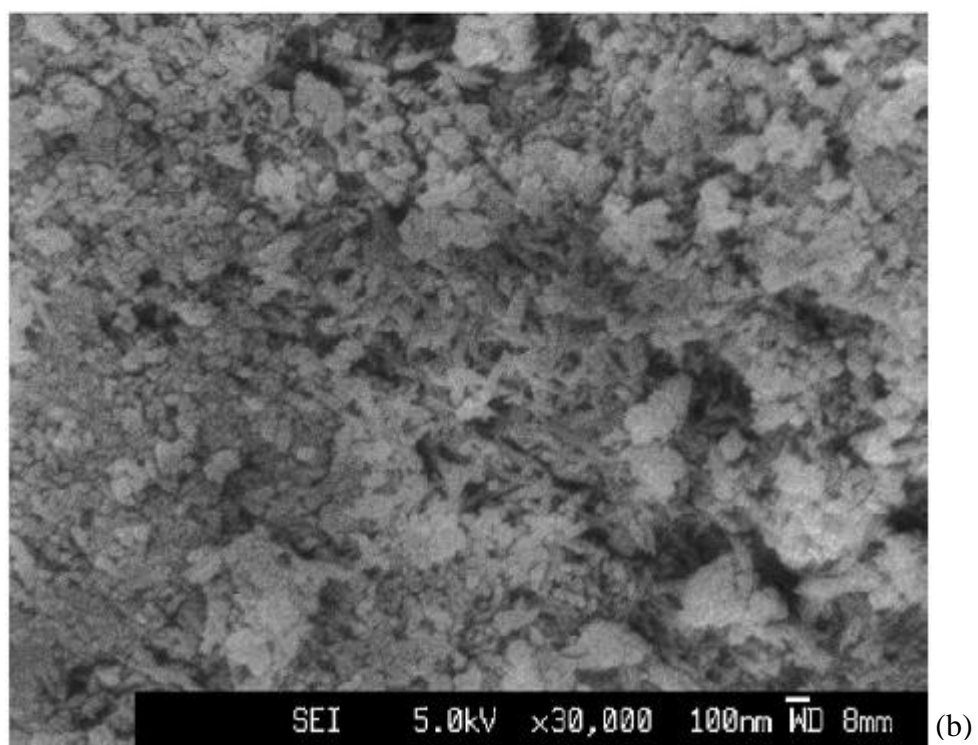
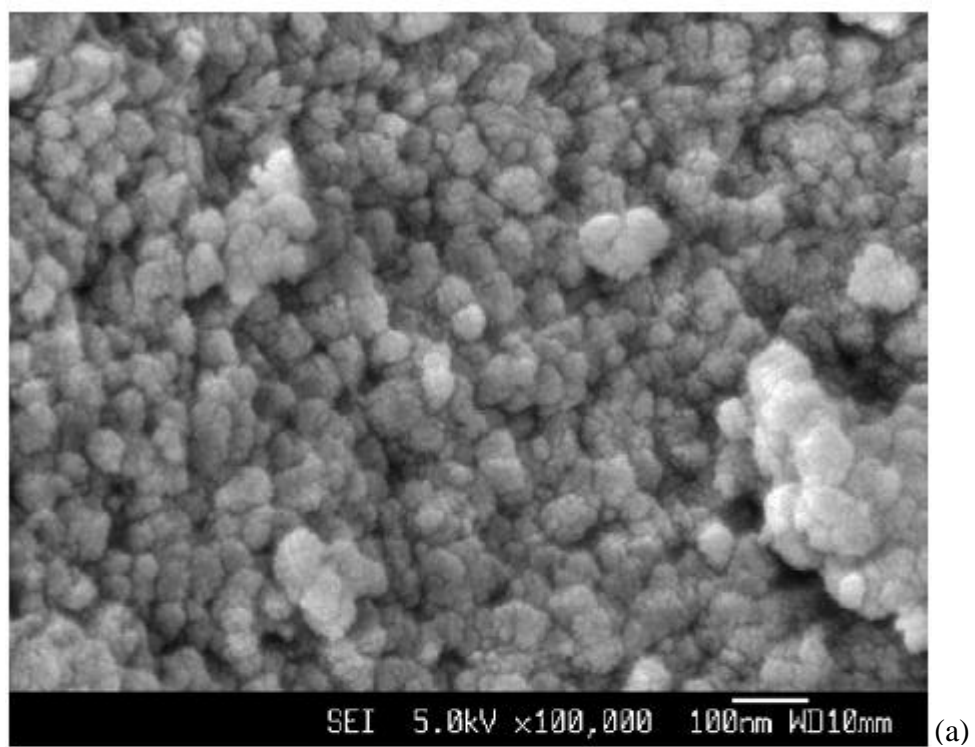


Fig. 1

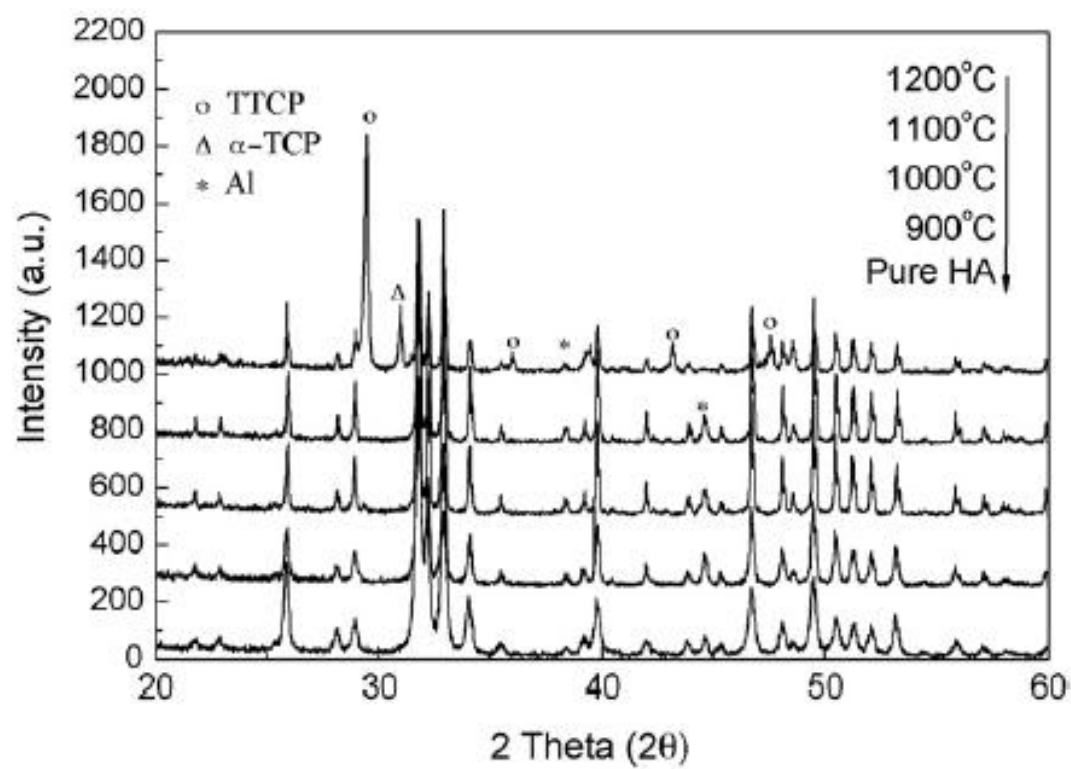


Fig. 2

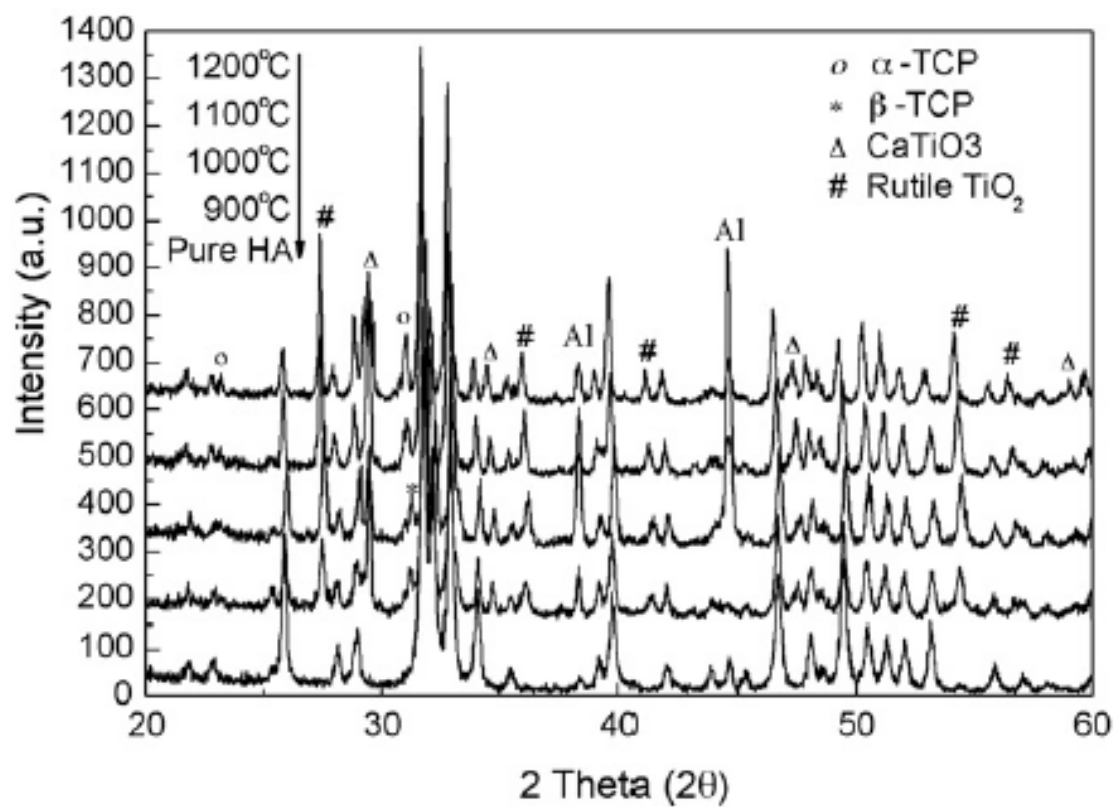


Fig. 3

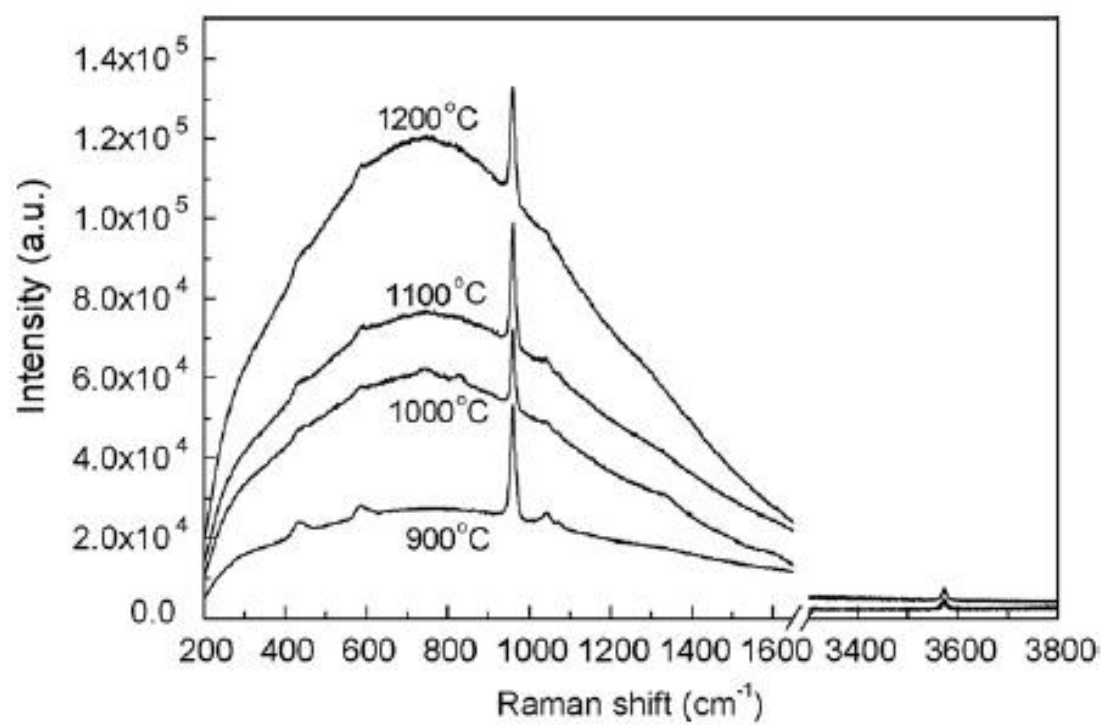


Fig. 4

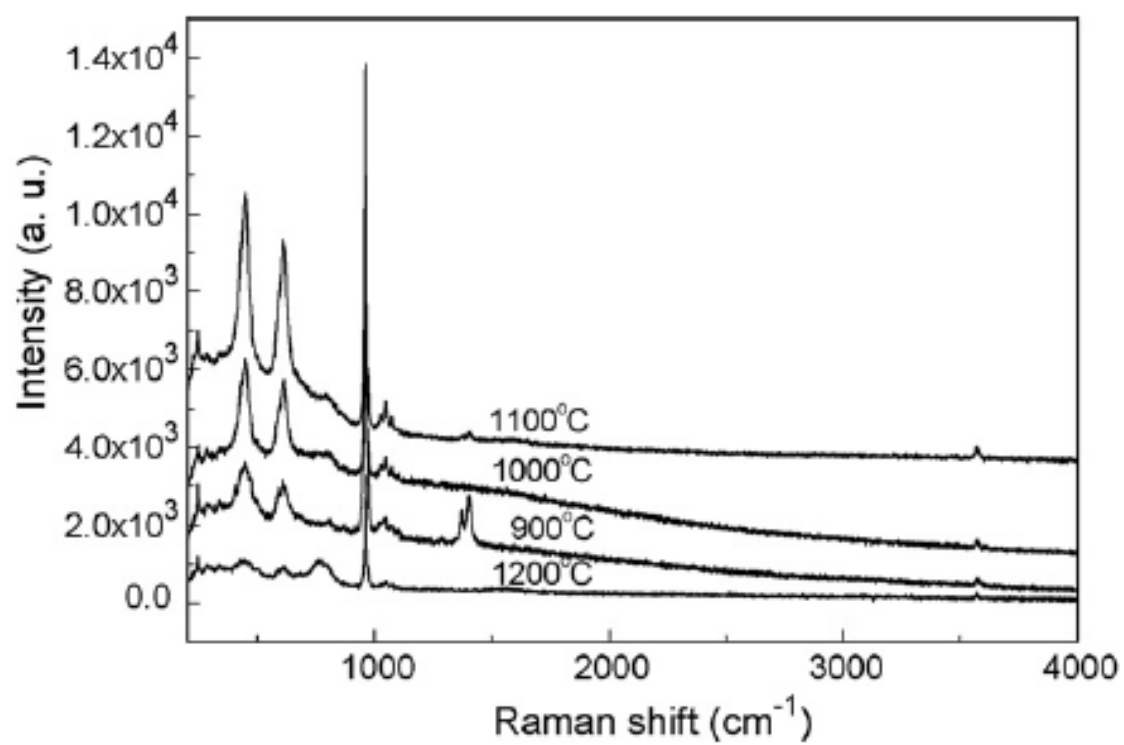


Fig. 5

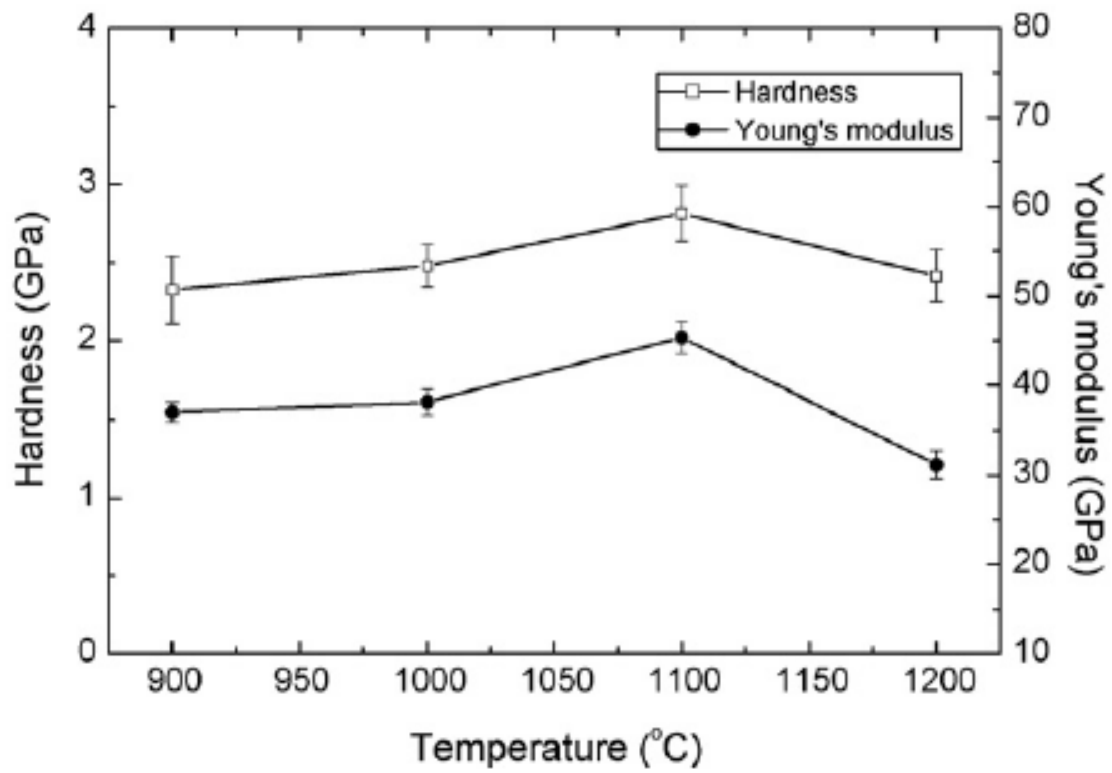


Fig. 6

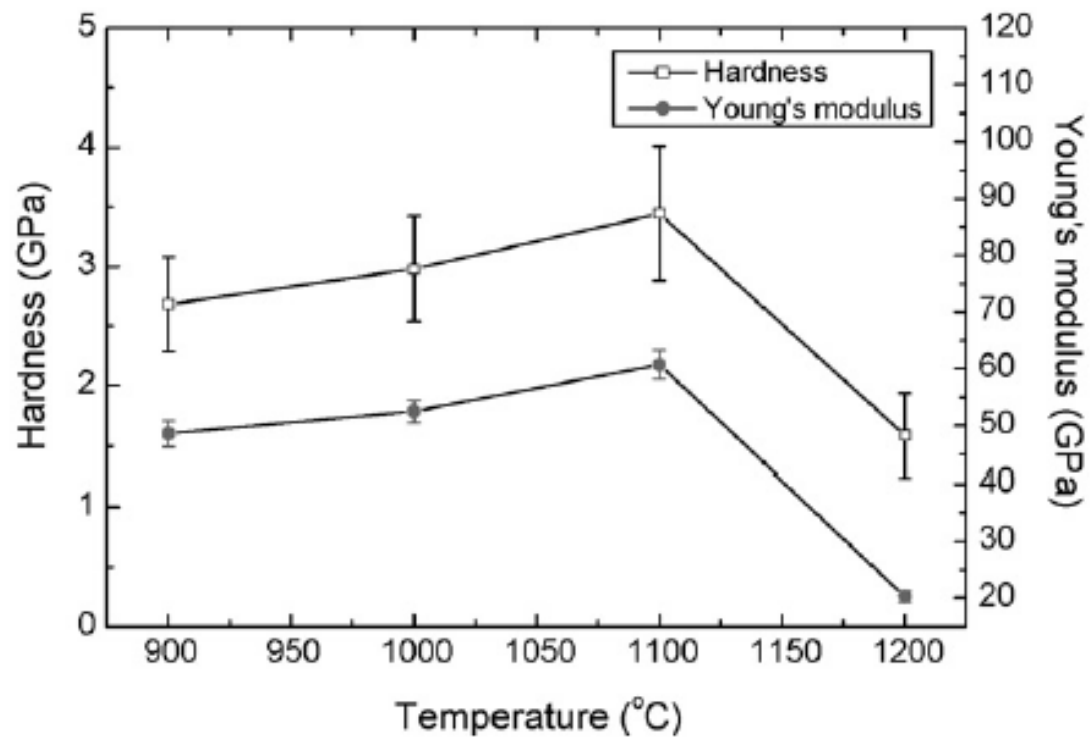
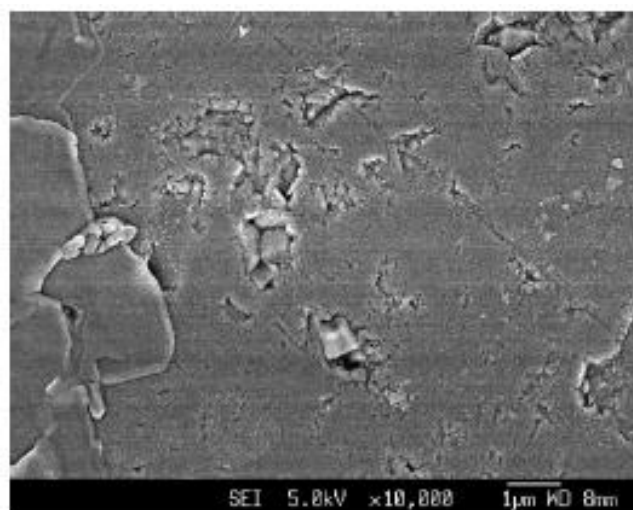


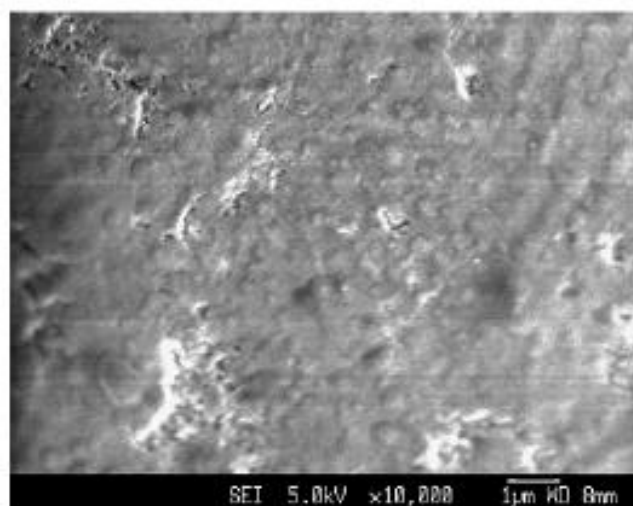
Fig. 7



900°C



1000°C



1100°C

Fig. 8

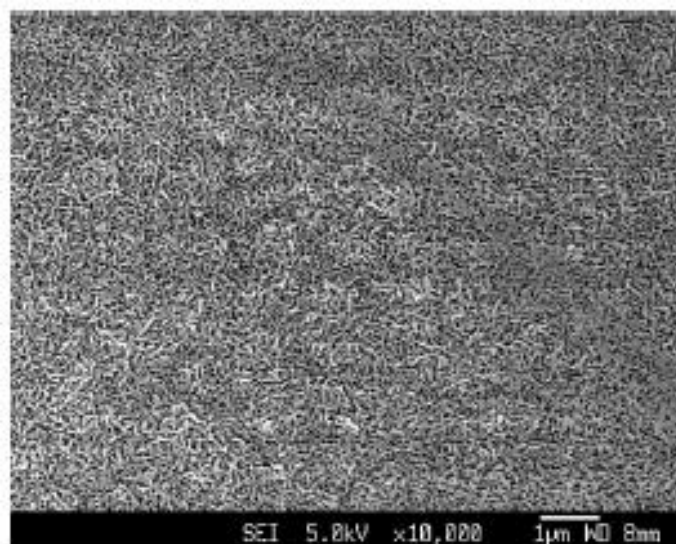


Fig. 9